Collision statistics of driven granular materials

Daniel L. Blair and A. Kudrolli

Department of Physics, Clark University, Worcester, Massachusetts 01610

We present an experimental investigation of the statistical properties of spherical granular particles on an inclined plane that are excited by an oscillating side wall. The data is obtained by high-speed imaging and particle tracking techniques. We identify all particles in the system and link their positions to form trajectories over long times. Thus, we identify particle collisions to measure the effective coefficient of restitution and find a broad distribution of values for the same impact angles. We find that the energy inelasticity can take on values greater than one, which implies that the rotational degrees of freedom play an important role in energy transfer. We also measure the distance and the time between collision events in order to directly determine the distribution of path lengths and the free times. These distributions are shown to deviate from expected theoretical forms for elastic spheres, demonstrating the inherent clustering in this system. We describe the data with a two-parameter fitting function and use it to calculate the mean free path and collision time. We find that the ratio of these values is consistent with the average velocity. The velocity distributions are observed to be strongly non-Gaussian and do not demonstrate any apparent universal behavior. We report the scaling of the second moment, which corresponds to the granular temperature, and higher order moments as a function of distance from the driving wall. Additionally, we measure long-time correlation functions in both space and in the velocities to probe diffusion in a dissipative gas.

PACS number(s): 81.05.Rm, 05.20.Dd, 45.05.+x, 45.70.Mg

I. INTRODUCTION

Granular material represent a type of matter not well defined by conventional means. Although each granular particle is obviously solid, an assemblage of these particles show distinctly nonsolid behavior when subjected to external forces [1]. In the rapid flow regime, the interaction between the grains is collisional and the system resembles a dense *granular gas*. Indeed, the kinetic theory for dense gases formulated by Chapman and Enskog [2] have been modified to include the dissipative nature of the collisions [3,4]. However, a number of approximations have to be made in any calculation that can be only validated by experiments. Furthermore, even if key assumptions such as equipartition breakdown [5–7], it is important to have a measure of the failure to guide further development.

Energy has to be constantly supplied from an external source to observe a steady state in granular gas systems. Therefore, model experiments consist of granular particles inside a container where energy is continuously injected at a side wall [8–10]. Thus gradients are present in experimental granular systems, which implies that care must be taken when comparing results to nonequilibrium kinetic theory [11–13]. With advances in high-speed image acquisition, it is now possible to obtain positions of particles several times between collisions. However, particle positions and velocities can be obtained accurately only in two dimensions by direct imaging thus forcing certain constraints on the geometry of the system.

One of the first such experiments to investigate velocity distribution functions (VDFs) utilized an apparatus in which particles are vibrated vertically inside a narrow transparent box [8,14,15]. Maxwellian statistics were reported for the vertical and horizontal velocity components of the particles parallel to the plane of the transparent side walls. Additional interactions in these systems arise due to collisions between particles and the side walls [14]. Following this work, Wildman, Huntly, and Hansen [16] were able to do long time particle tracking to measure diffusion constants by interpreting mean square displacement data over a very broad range of density. More recently, in a similar apparatus, Rouyer and Menon [17] report that their VDFs have a universal form that can be parametrized by a single variable, the granular temperature. A different method of energy injection utilizes large flat container that is vibrated vertically to excite a sub mono layer of particles [10,18,19]. The velocity of the particles in the horizontal plane are measured and are found to follow a non-Gaussian distribution. However, the impact of the velocity gradient in the vertical direction on the observed distributions are not taken into account because these components cannot be measured.

Our experiment is a variation of the vertically vibrated apparatus. Spherical particles are constrained to roll on an inclined two-dimensional surface. This geometry allows for a direct investigation of the interplay between energy injected at the side wall and the dissipation through inelastic collisions. In addition, the inclination reduces the effects of gravity, therefore minimizing shock waves. This system has been used to demonstrate clustering and collapse when the interparticle collision frequency is much greater than particle-driving wall collision frequency [9]. Recent works have explored a full range VDFs, from very near Gaussian behavior to highly non-Gaussian distribution functions, as well as velocity correlations [20,21].

In addition to analytical techniques and experiments, several groups have utilized computer simulations of inelastic hard spheres with both Molecular Dynamics [12,22–27] and Direct Simulation Monte Carlo [28–32] techniques to investigate the statistical properties of granular gases. Using DSMC simulations, Baldassarri *et al.* [30] have found veloc-

ity and density distributions that are qualitatively similar to our previous experimental results [21]. Recent work by Brey and Ruiz-Montero [27] investigate how the second and fourth moments of the VDFs scale as a function of distance from the driving wall, which until now, have not been experimentally tested.

In this paper, we report on the statistical properties of a gas of inelastic particles constrained to two dimensions. An inclined geometry reduces the gravitational acceleration acting on each particle which results in lower mean velocities. The combination of slow dynamics and high-speed imaging allows us to accurately identify the particle trajectories and collision events. By using velocities before and after a collision event, we measure the normal coefficient of restitution. We find that these quantities are found to be broadly distributed for the same impact parameters. By calculating the distance and time between collision events we measure the distributions of free paths and times. We find that these distributions do not follow the result found from kinetic theory. The path and time distributions have an overpopulation of short distance and time bins, demonstrating the inherent clustering present in granular gases. We propose an empirical form that captures the distributions, which is then used to calculate the mean free path and free time as a function of density. The particle trajectories are also used to measure the mean square displacement, velocity autocorrelation, and diffusion rates. The distribution of particle velocities are measured with a variation in density of an order of magnitude and show distinctly non-Gaussian behavior with no apparent universal form. We compare our results to recent experiments, as well as theoretical and simulation treatments of equivalent systems.

The paper has the following structure. In Sec. II we present the experimental apparatus and imaging methods. Section III provides the overall system characteristics such as the density distributions and coefficients of restitution and inelasticities. We then present our analysis of the trajectories of the particles in Sec. IV. Finally, in Sec. V we summarize our results in the context of granular kinetic theory and simulations.

II. EXPERIMENTAL METHODS

The experimental configuration [Fig. 1], consists of a $100\sigma \times 60\sigma$ (31 cm $\times$ 19 cm) glass plane that is inclined at an angle β with the horizontal. The particles are stainless steel with diameter $\sigma = 3.175$ mm and a high degree of sphericity ($\delta\sigma/\sigma = 10^{-4}$). The number of particles, measured in number of monolayers N_l across the driving wall, is varied between $N_l = 1-5$ in steps of one layer, (viz., from $N_p = 100-500$ in steps of 100, where N_p is the number of particles). The energy source is an oscillating side wall, driven by a solenoid, that is located as shown in Fig. 1(a). The driving signal is a 10 Hz pulse with a velocity during each pulse of ~ 40 cm s^{-1}. The driving frequency and amplitude were chosen to ensure that no phase dependence on the center of mass is observed (at frequencies below 2 Hz the particle positions are phase locked with the driving). The signal is produced with a computer interfaced Aglient Technologies
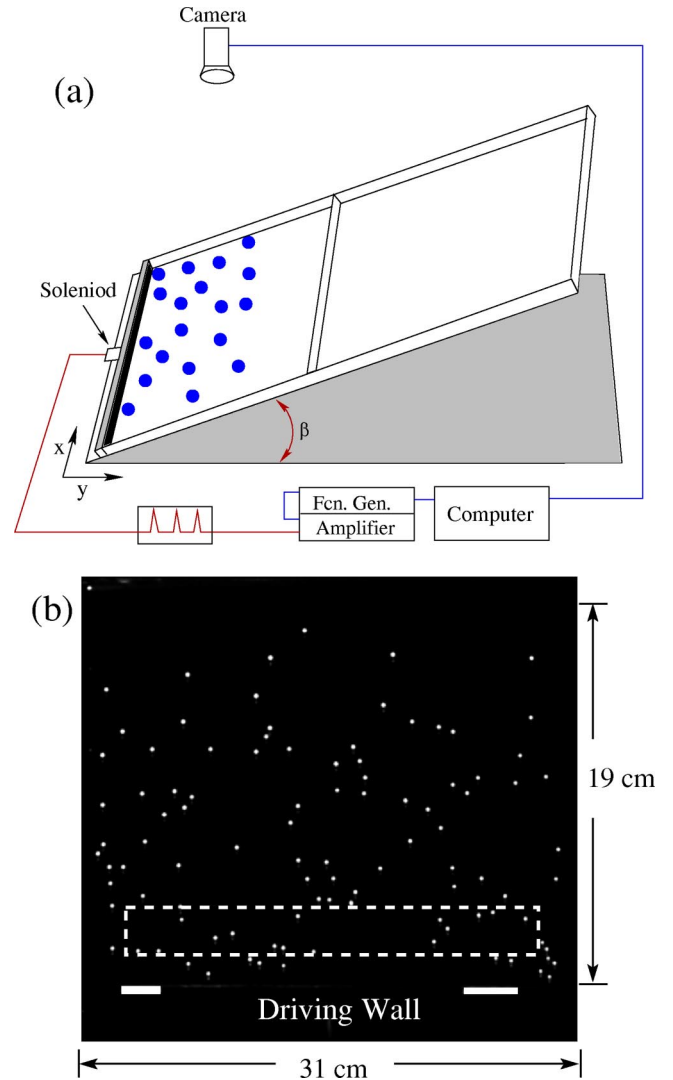

FIG. 1. (Color online) (a) Schematic diagram of the experimental setup. The inclined plane is a smooth glass surface, the side walls and driving wall are stainless steel so that the particle-boundary collisions approximate those between particles. The driving is produced by a solenoid connected to the lowest side wall. The angle of inclination β, can be varied from $\beta = 0° - 8°$, the values of β we have chosen are $2° \pm 0.1°$ and $4° \pm 0.1°$. (b) An image of the system taken from above. The bottom right corner is considered the origin of our coordinate system (0,0). The white bars allow us to track the position of the driving wall.

33120-A wave-form generator that is and subsequently amplified by an HP 6824A Amplifier. The inclination of the plane can be varied between $\beta = 0° - 8°$, for our experiments the angle was fixed at $\beta = 2° \pm 0.1°$ or $4° \pm 0.1°$. In the extreme case of $\beta \ll 1°$, the particles essentially cease to interact with the energy source and cluster at the side opposite of the driving.

The particles are imaged using a Kodak MotionCorder SR1000 high-speed digital camera. We measure the positions of all particles contained in the apparatus for 1365 frames at 250 frames per second at full spatial resolution of 512×480 pixels. These digital images are then transfered to a computer and analyzed using a centroid method that allows
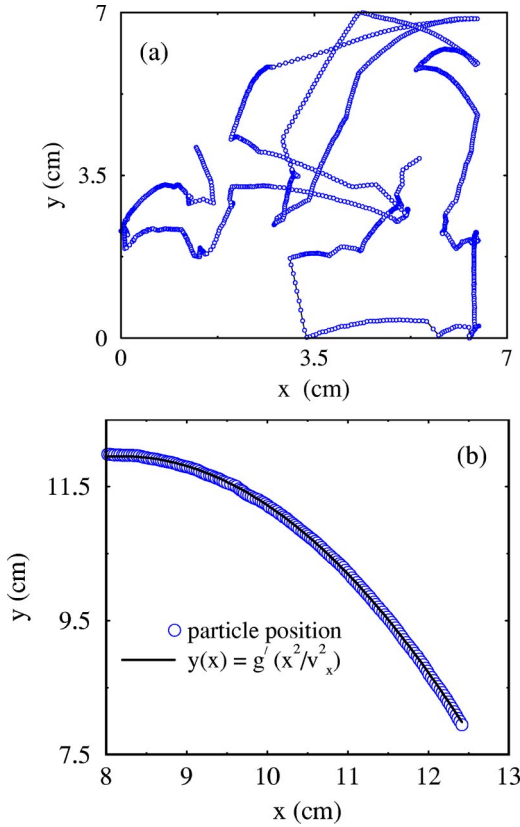
FIG. 2. (Color online) (a) Linked particle positions over 1365 time steps ($N_l=3$). We can determine particle collision events with a high degree of accuracy from trajectories such as this. (b) The parabolic path of a particle. We use fixed values for v_x and g $=980$ cm s^{-2} to measure $g'=\frac{5}{7}g \sin \beta$. The fit gives $\beta=2.2°$, the deviation from the measured value of β is 9%.

us to resolve each particle to subpixel accuracy. After each particle is located the positions are then connected in time to form continuous trajectories for 5.46 s. Our coordinate system is such that the x,y axes are parallel and perpendicular to the driving, respectively [see Fig. 1]. A typical particle trajectory is shown in Fig. 2(a). Multiple collision events can be distinguished with nearly straight paths between each event. A particle that freely rolls on the inclined plane will follow a parabolic trajectory [see Fig. 2(b)]. The particle trajectory is given by

$$y(x) = \frac{5}{7} \frac{x^2}{2v_x^2} g \sin(\beta), \qquad (1)$$

where g is the acceleration due to gravity, v_x is measured from the width of the parabola, and the $\frac{5}{7}$ factor is due to the moment of inertia for a solid sphere.

III. SYSTEM CHARACTERISTICS

A. Density distributions

The results presented will be given in terms of the number of single layers across the cell, N_l and the angle of inclination β, which determine the area fraction ϕ [see Table I]. We

TABLE I. Experimental values of the number of layers N_l, the angle of inclination β, and the resulting measured value of ϕ. N_p, the number of particles in the system, is given for clarity.

N_l	β	ϕ	N_p
1	2.0	0.022	100
2	2.0	0.068	200
3	2.0	0.138	300
4	2.0	0.191	400
4	4.0	0.302	400
5	4.0	0.581	500

measure ϕ by defining a region of interest (ROI) that is centered about the peak in $\rho(y)$, [Fig. 3(b)] whose extent in the y direction is limited to $\pm 10\%$ of $\rho(y)$. The ROI scheme excludes all particles that are within 3σ of the side walls to
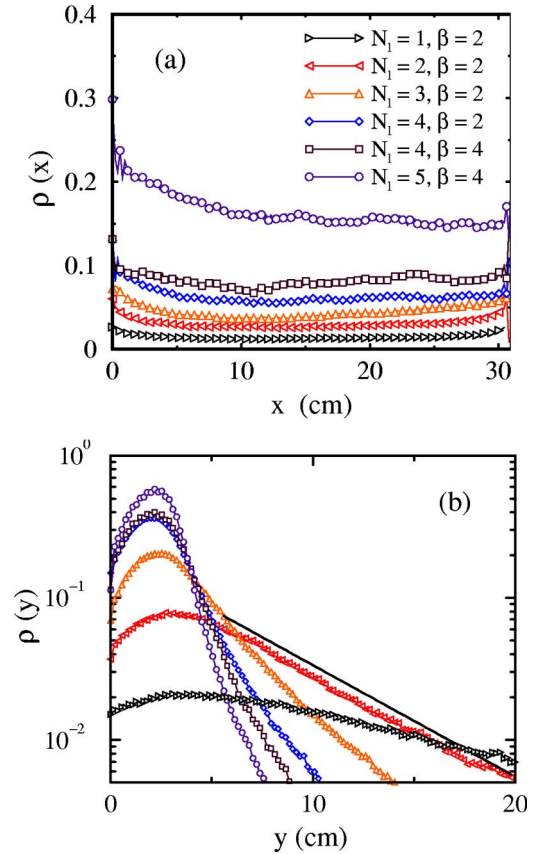

FIG. 3. (Color online) (a) The density $\rho(x)$ versus x for all N_l. The obvious clustering due to inelastic collisions at the side walls is demonstrated here. Also, as N_l is increased the system becomes more inhomogeneous across the cell. This effect is most likely due to the onset of clustering instabilities that have been recently discussed [33–35]. (b) The aerial density plots $\rho(y)$ for each N_l and β on a log-linear plot. The density ϕ is measured in a particular area by integrating $\rho(y)$ over that region of interest. The total under each curve corresponds to the average area fraction for that particular N_l. The solid line shows an exponential fit over the tail of the distribution of $N_l=200$. However, we will demonstrate that the isothermal atmosphere is not obeyed for any density.

ensure that clustering due to the side walls does not affect our results [see Fig. 3(a)]. The over-plotted box in Fig. 1(b) demonstrates the ROI definition for $\phi=0.13$. A more stringent division of the system in the y direction will be used when the behavior of the temperature, pressure, and kurtosis are discussed in Sec. IV. The form of the density in the y direction is similar to that found in Refs. [14,36]. However, we find that the form of the tails of $\rho(y)$ at higher values of $N_l \beta$ deviate from Boltzmann distribution. This implies that the law of isothermal atmospheres breaks down for granular systems as we shall also see when we discuss the scaling of the granular temperature in Sec. IV E.

B. Particle collisions

We identify collision events from the trajectories by using the following algorithm. Velocities are constructed as finite differences $\mathbf{v}_j = \Delta\mathbf{x}/\Delta t$, where $\Delta\mathbf{x} = \mathbf{x}(t_j) - \mathbf{x}(t_i)$ and the subscripts i,j represent positions separated by the time difference $\Delta t = 4$ ms. All velocity vectors are compared sequentially to find direction changes given by

$$\psi = \cos^{-1}(\hat{\mathbf{v}}_i \cdot \hat{\mathbf{v}}_j), \tag{2}$$

where $\hat{\mathbf{v}} = \mathbf{v}/|\mathbf{v}|$ the unit vector of the calculated velocity. If $20° \leq \psi \leq 180°$ the proximity of all particles at the same time instant is checked. If a particle is found within a radius $\sigma + \Delta\sigma$, whose velocity also satisfy Eq. (2) it is considered as a candidate for a collision. To assure that recollisions are not occurring, we maintain a record of the identity of the previous collision partner. We then ensure that those particles can recollide if and only if the partner particle has undergone a collision with yet a third particle. If particles pass these requirements then a collision has occurred. To extend the algorithm to include collisions with the boundary walls we first check if Eq. (2) is satisfied. We then check if the particle's center is within $\sigma + \Delta\sigma$ of a boundary and it's velocity component perpendicular to the wall is reversed.

C. Coefficient of normal restitution

The loss of energy in a collision is determined by the coefficient of restitution. If particles are rough, (i.e., frictional) both the the normal and tangential components must be considered when describing inelastic particle collisions. Using simulations and theory, McNamara and Luding [37] have described the lack of energy equipartition between the linear and rotational degrees of freedom for colliding rough particles. As described in Sec. II, the particles in our system must roll between collision events, which leads to complex interactions at contact [38]. Angular momenta, (both from spin induced by the substrate and about the normal induced by collisions) cannot be resolved experimentally. Therefore, while we can observe the effect of the subtle interplay between the transference of linear and angular momenta during collisions, we cannot resolve the contribution to each degree of rotational freedom. This implies that the values of the coefficient of normal restitution and inelasticities presented below are *effective* quantities.
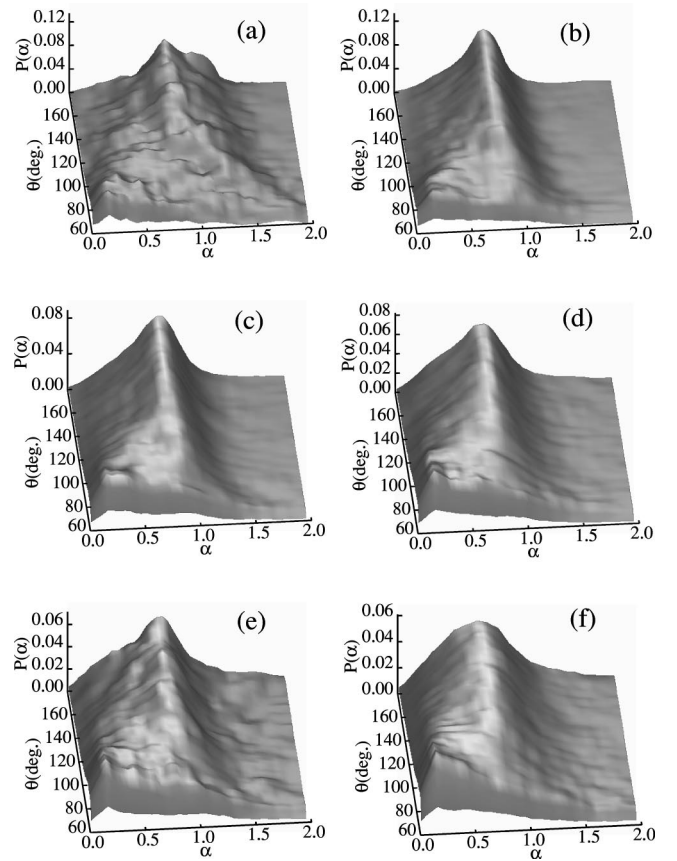

FIG. 4. The distribution of the normal component of restitution α versus $60° \leq \theta \leq 180°$, the relative angle of incidence between particle velocities. (a) $N_l = 1$, $\beta = 2.0$, (b) $N_l = 2$, $\beta = 2.0$, (c) $N_l = 3$, $\beta = 2.0$, (d) $N_l = 4$, $\beta = 2.0$, (e) $N_l = 4$, $\beta = 4.0$, (f) $N_l = 5$, $\beta = 4.0$. The value of the z axis for each graph is the probability of a collision giving a value of α in a range of $\theta + \Delta\theta$, where $\Delta\theta = 2°$

Two smooth particles that undergo an inelastic collision with a relative velocity between particles $\mathbf{v}_{12} = \mathbf{v}_1 - \mathbf{v}_2$, will obey the reflection law $\mathbf{v}_{12}^* \cdot \hat{\sigma} = -\alpha\mathbf{v}_{12} \cdot \hat{\sigma}$, where α is the normal component of the restitution coefficient and $\hat{\sigma}$ is the unit vector connecting the centers of the particles. Having an efficient method for collision identification, we are able to measure the relative velocities of two particles before and after collision events. The coefficient of normal restitution during a binary collision is given by

$$\alpha = -\frac{(\bar{\mathbf{v}}_{12}^* \cdot \hat{\sigma})}{(\bar{\mathbf{v}}_{12} \cdot \hat{\sigma})}, \tag{3}$$

where the overbar denotes average over three precollisional or postcollisional velocities measured in the ROI described above [see Fig. 1(b)]. The angle between the relative velocities of two colliding particles is given by

$$\theta = \cos^{-1}(\bar{\mathbf{v}}_{12} \cdot \bar{\mathbf{v}}_{12}^*). \tag{4}$$

Thus we can characterize the coefficient of restitution as a function of θ. The probability distributions $P(\alpha)$ for $60°$
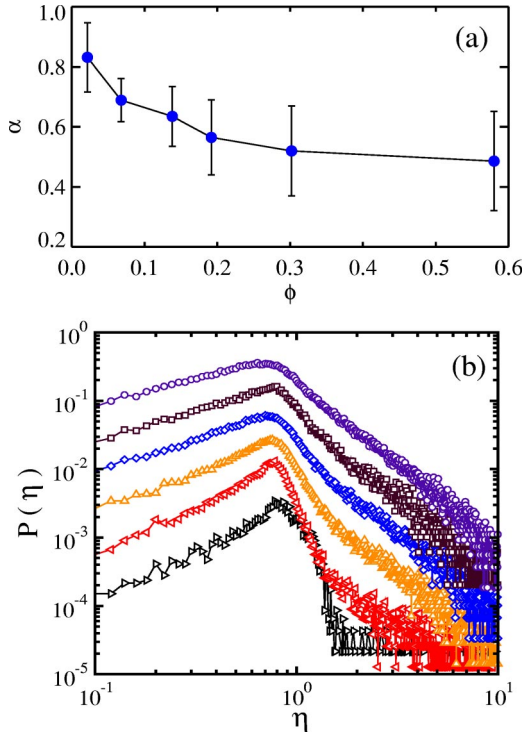
FIG. 5. (Color online) (a) The mean value of the distributions of α shown in Fig. 4 averaged over $60° \geqslant \theta \geqslant 180°$, as a function of the average covering fraction ϕ. The bars indicate the spread in the distribution (b). The distribution of energy inelasticities given by Eq. (5) for ($\triangleright$) $N_l = 1$, $\beta = 2.0$, ($\triangleright$) $N_l = 2$, $\beta = 2.0$, ($\triangleright$) $N_l = 3$, $\beta = 2.0$, ($\diamond$) $N_l = 4$, $\beta = 2.0$, ($\square$) $N_l = 4$, $\beta = 4.0$, ($\circ$)$N_l = 5$, $\beta = 4.0$. Each distribution is shifted vertically for clarity.

$\leqslant \theta \leqslant 180°$ for each $N_l \beta$, are shown in Figs. 4(a)-4(f). Data for $\theta < 60°$ suffers from a lack of statistics and therefore is not included. Each graph represents the probability of the inelasticity having a value α for a range of $\theta + \Delta\theta$, where $\Delta\theta = 2°$. $P(\alpha)$ follows a very broad distribution of values over all θ, and have a decreasing mean value as function of ϕ [see Fig. 5(a)]. Thus we find that the coefficient of restitution can have a broad distribution of values for the same impact angle.

We also measured the energy loss due to a collision as a function of $N_l \beta$. The ratio of the magnitudes of the relative velocities before and after a collision,

$$\eta = \frac{|\bar{\mathbf{v}}_{12}^*|}{|\bar{\mathbf{v}}_{12}|}, \tag{5}$$

determines the *energy* restitution coefficient, ($\eta^2 = \alpha^2$ if all θ are averaged). Figure 5(b) shows the distributions of measured values of η shifted for clarity. We find that a peak exists at a value that is consistent with α^2. Furthermore there exists a power-law tail for values of $\eta > 1$, which has been interpreted as a *random inelasticity* [39]. The appearance of a tail at high η implies that the rotational degrees of freedom are actively transferring energy to translational motion during a collision.
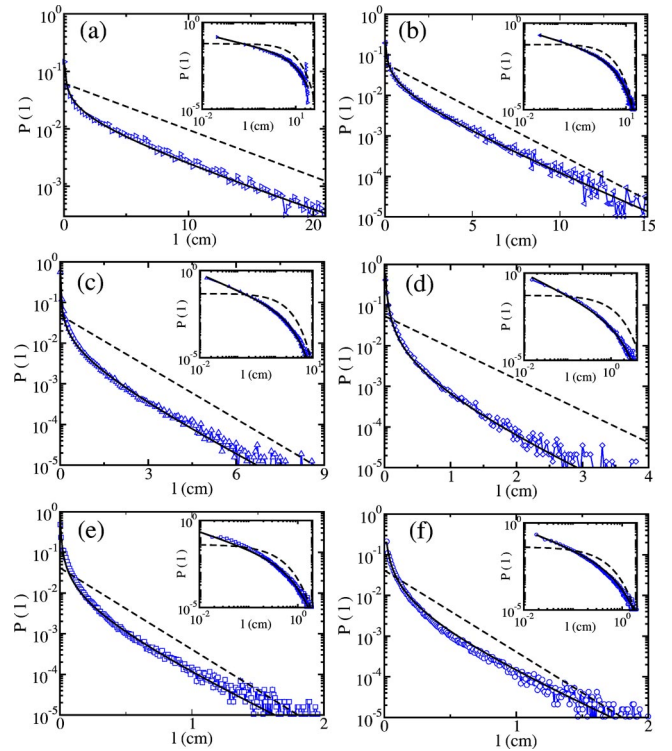

FIG. 6. (Color online) The probability distributions of path lengths $P(l)$ versus l, on a log-linear scale, and *inset* log-log scale (a) $N_l = 1$, $\beta = 2.0$, (b) $N_l = 2$, $\beta = 2.0$, (c) $N_l = 3$, $\beta = 2.0$, (d) $N_l = 4$, $\beta = 2.0$, (e) $N_l = 4$, $\beta = 4.0$, (f) $N_l = 5$, $\beta = 4.0$. The dashed line shows the theoretical form given by Eq. (6) derived for elastic particles, and the solid line is an empirical fit given by Eq. (7a). Table II shows the fit parameters.

IV. RESULTS

A. Distributions of paths and times

We measure the distribution of paths lengths from the the geometric distance between collision events defined in our ROI at each $N_l \beta$ [Figs. 6(a)-6(f)]. By basic kinetic theory arguments [40], the distribution of path lengths for an elastic hard-sphere gas (and by a similar treatment the distribution of free times) is given by

$$P(l) = (2\sqrt{2}\phi)e^{-2\sqrt{2}\phi l}. \tag{6}$$

The distribution therefore should follow a simple exponential form depending only on the density. However, it is clear from the dashed lines in Figs. 6(a)-6(f) that the simple form given by Eq. (6) does not describe the behavior over all l.

The distributions of times between collisions $P(\tau)$ [Figs. 7(a)-7(f)] is also measured and shows similar behavior to that of the path length distributions, that is an overpopulation of the short-time bins. This should be expected from the simple relationship between the displacement and the time. However, it is worth noting to mention that the ratio of l/τ versus the path length l, is not a constant over all values of l, implying that the average speed of the system depends on the distance or time between collisions. Elastic hard spheres will have a mean free path that is simply $\bar{l} = \bar{v}\bar{\tau}$, where $\bar{v}$ and $\bar{\tau}$
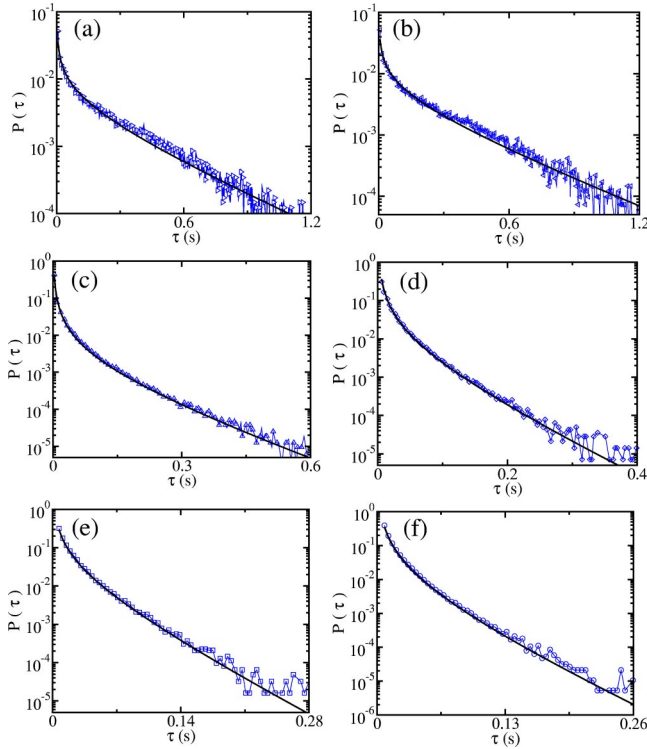
FIG. 7. (Color online) The probability distributions of free times $P(\tau)$ versus τ, on a log-linear scale (a) $N_l=1$, $\beta=2.0$, (b) $N_l=2$, $\beta=2.0$, (c) $N_l=3$, $\beta=2.0$, (d) $N_l=4$, $\beta=2.0$, (e) $N_l=4$, $\beta=4.0$, (f) $N_l=5$, $\beta=4.0$. The solid line is a fit given by Eq. (7b).

TABLE II. Fitting parameters for Eqs. (7a) and (7b). The values are arranged $a(a)$ for $P(l)[P(\tau)]$, respectively. The $(\cdots)$ correspond to the values for $P(\tau)$.

N_l	β	$a(a)$	$b(b)$	$c(c)$
1	2	0.031(0.0027)	0.428(0.511)	0.154(2.969)
2	2	0.025(0.0025)	0.603(0.665)	0.393(6.024)
3	2	0.008(0.0003)	0.932(1.203)	0.742(8.306)
4	2	0.003(0.0008)	1.258(1.209)	1.489(16.91)
4	4	0.002(0.0002)	0.970(1.043)	3.171(26.45)
5	4	0.002(0.0005)	1.096(1.384)	2.887(28.33)

$$\bar{v}=\frac{\bar{l}}{\bar{\tau}}=\frac{\int_0^\infty lP(l)dl}{\int_0^\infty \tau P(\tau)d\tau},\qquad(8)$$

and compared that to the average of the speed distribution $\langle v_{x,y}\rangle$ in the same ROI. Figure 8 shows both the measurements for all $N_l\beta$. The agreement is within 10% over the entire range of $N_l\beta$ indicating that the proposed forms in Eqs. (7a) and (7b) quantitatively capture the behavior of the distributions.

B. Velocity autocorrelation

The velocity autocorrelation function (VAF) is computed for the x components of the velocities within an ROI by using the following [41]:

$$C_v(t)=\frac{1}{N_pN_st_{max}}\sum_{i,j=0}^{N_p,N_s}\sum_{\Delta t=1}^{t_{max}}\mathbf{v}_{ij}(t_o)\cdot\mathbf{v}_{ij}(t_o+\Delta t),\quad(9)$$

where N_s is the total number of data sets, N_p is the number of particles and t_{max} is the total number of time origins. Figure 9(a), shows the measured values of the VAF normalized by $\langle\mathbf{v}(0)^2\rangle$ in our system.

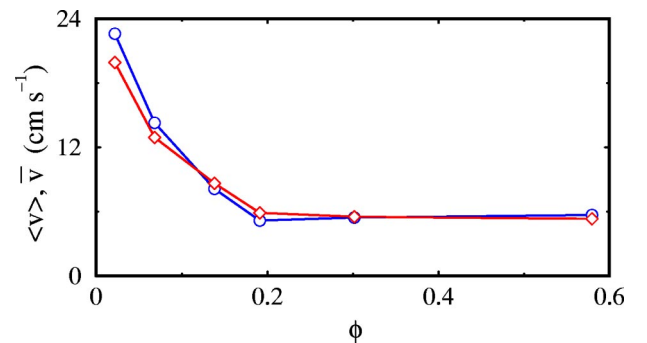In simulations of hard-sphere fluids, Alder and Wainwright [42] first found that the form for the VAF was

are the average speed and collision time, respectively. Also, the mean free path can be derived directly from the distribution of path lengths, $\bar{l}=\int_0^\infty lP(l)dl$, where $P(l)$ is given by Eq. (6). Grossman, Zhou, and Ben-Naim [6] have interpolated how the mean free path for a granular system should be modified to account for higher collision rates due to increased density. Although the interpolation gives a qualitatively accurate correction for passing between the high and low density limits, the actual distribution of path lengths has not been measured or calculated for a granular gas.

We have found an empirical form that well describes the measured distributions of path lengths and free times,

$$P(l)=a(l)^{-b}e^{-cl},\qquad(7a)$$

$$P(\tau)=a(\tau)^{-b}e^{-c\tau},\qquad(7b)$$

where a,b,c for the path lengths and free times are shown in Table II for all $N_l\beta$. This form appears to capture both the short l and τ power-law behavior. In the dilute case the form returns to the theoretical prediction for larger path lengths.

From the distribution of path lengths and free times, we calculate the mean free path and time by utilizing the fitting form and its parameters. The ratio of the mean free path to the mean collision time should determine the average speed $\bar{v}$ in the ROI where the distributions are measured. We have taken the ratios of the integrated distributions,

FIG. 8. (Color online) The average speed measured for each $N_l\beta$. (○) $\bar{v}$ obtained from Eq. (8), and (◇) $\langle v\rangle$ measured from the mean of the speed distribution. The two independent measures give similar values over the entire density range.
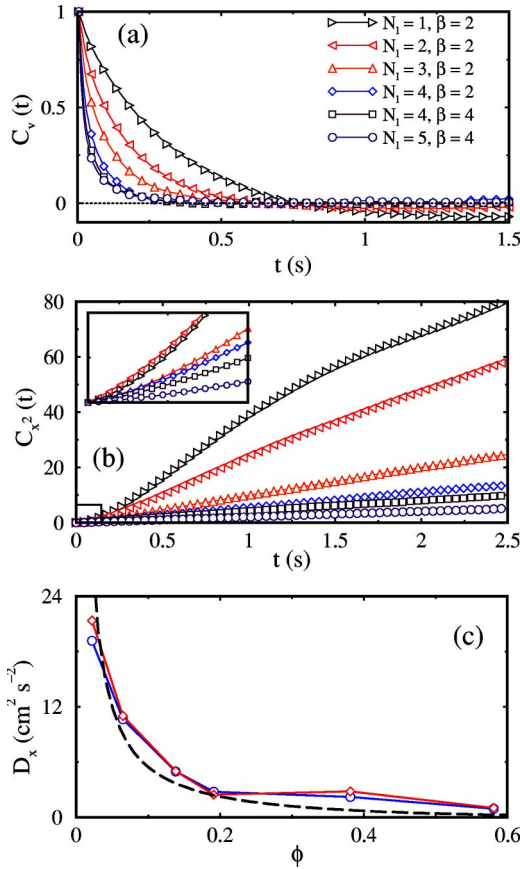
FIG. 9. (Color online) (a) The velocity autocorrelation function $C_v(t)$. (b) The mean square displacement in the x direction for each $N_l\beta$ for $t=0-2.5$ s. *Inset:* the short time behavior indicated by the box in the main figure. (c) The diffusion constants calculated for each ϕ, where ($\bigcirc$) corresponds to the numerical integration of C_v from (a), and ($\diamondsuit$) corresponds to the least squares fit of C_{x^2} from (b). The dashed line shows the kinetic theory result for a fixed temperature, which is given by the average measured value over this range of ϕ.

strongly depended on the density of the system. For very low densities the characteristic form of the correlation function was given simply by

$$C_v(t) = \langle \mathbf{v}(0)^2 \rangle e^{-t/\tau_E}, \tag{10}$$

where τ_E is the Enskog collision time. If the density of the system is increased however, the form of Eq. (10) breaks down and $C_v(t)$ can become negative with long range tails due to the caging of particles by their neighbors. We find, that the *lowest* density case becomes, and remains negatively correlated after the decay from $\langle \mathbf{v}(0)^2 \rangle$ [Fig. 9(a)]. This appears to be in contradiction with Ref. [42] but is due to a finite-size effect. That is, the particles are interacting frequently with the side walls at low densities, which reverse the sign of velocity vectors, thus leading to the observed anticorrelation. The predominance of the sidewall interactions are screened for the intermediate densities due to the increased number of particle-particle collisions, therefore no anticorrelations are observed.

C. Mean square displacement

To determine the mean square displacement of the x component of the particle positions [Fig. 9(b)], by using the sequential time zeros for each trajectory [41] given by

$$C_{x^2}(t) = \frac{1}{N_p N_s t_{max}} \sum_{i,j=0}^{N_p,N_s} \sum_{\Delta t=1}^{t_{max}} |\mathbf{x}_{ij}(t_o) - \mathbf{x}_{ij}(t_o + \Delta t)|^2, \tag{11}$$

where N_s is the total number of data sets, N_p is the number of particles, and t_{max} is the total number of time origins. For these measurements, the ROI is allowed to increases in size along the y direction as N_l decreases. We have chosen to make this increase to ensure that particles at low N_l have had the opportunity to undergo a collision while under consideration.

The long time behavior of C_{x^2} for each $N_l \beta$ [Fig. 9(b)], displays linear dependence on time, indicating diffusive behavior. However for $N_l = 1$, C_{x^2} clearly shows a crossing from one linear regime to another, which may be a possible indication of finite system size for low density. For short times, [Fig. 9(b) *inset*] the behavior is ballistic as indicated by the quadratic increase of C_{x^2} in time. As N_l is increased, the range of the ballistic regime dramatically decreases indicating a decrease in the Enskog collision time τ_E. The ballistic and diffusive regimes are consistent with what is expected for kinetic theory of elastic, finite-sized particles.

D. Self-diffusion

The self-diffusion constant D, can be determined for a system of particles by either evaluating the time integral of the velocity autocorrelation function,

$$D = \int_0^\infty C_v(t)dt, \tag{12}$$

or using the relationship between the mean square displacement of the particles and time over long times,

$$D = \lim_{t \to \infty} \frac{1}{2dt} C_{x^2}(t), \tag{13}$$

where d is spatial dimension. From kinetic theory [40], the diffusion constant of a two-dimensional gas is calculated as

$$D = \frac{\sigma}{8\phi g(\sigma)} \left(\frac{\pi T}{m} \right)^{1/2}, \tag{14}$$

where $g(\sigma)$ is the radial correlation function at contact [43] given by

$$g(r=\sigma) = \frac{16-7\phi}{16(1-\phi)^2}. \tag{15}$$

By numerically integrating the curves in Fig. 9(a), and performing a least squares fit to the data in Fig. 9(b) after the ballistic regime, we obtain the self-diffusion constant [see Fig. 9(c)]. We find that the values for the self-diffusion from
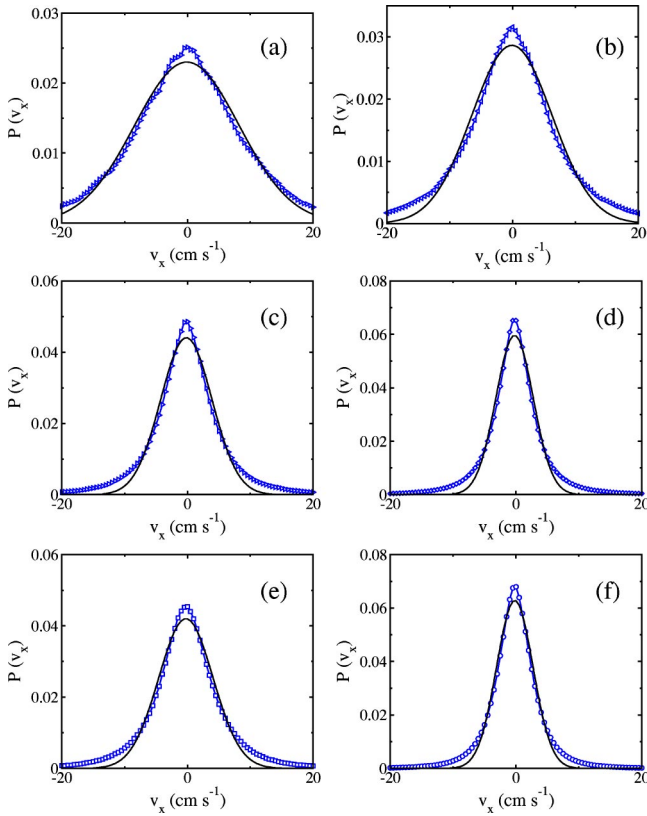
FIG. 10. (Color online) The velocity distribution functions $P(v_x)$ versus v_x on a linear-linear scale. (a) $N_l=1$, $\beta=2.0$, (b) $N_l=2$, $\beta=2.0$, (c) $N_l=3$, $\beta=2.0$, (d) $N_l=4$, $\beta=2.0$, (e) $N_l=4$, $\beta=4.0$, (f) $N_l=5$, $\beta=4.0$. The solid curves are a least squares fit to a Gaussian form given by Eq. (17). Note that the deviation from a Gaussian distribution extends all the way to the lowest velocity bins. Each distribution corresponds to $\sim 2\times 10^6$ unique velocities that are found within the ROI defined in the text.

Eqs. (12) and (13) are self-consistent. The solid line in Fig. 9(c) shows the form of Eq. (14) with the temperature T given by the granular temperature. The granular temperature is defined by

$$T_{x,y}=\frac{1}{2}m[\langle v_x^2\rangle+\langle v_y^2\rangle],\qquad(16)$$

where m is the mass of the particles and $\langle\cdots\rangle$ denote averages over the component distributions [see Sec. IV E]. The other constants in Eq. (14) are determined from system parameters. The theory for the diffusion of elastic particles, given by Eq. (14) closely matches our results for all ϕ. Thus we show that the effects of inelasticity on the self-diffusion are small.

E. Velocity distributions

The distribution of the x and y components of the particle velocities are plotted in Figs. 10(a)-10(f)–12(a)-12(f). The distributions correspond to velocities that are measured within a region of interest. The ROI is defined by making a narrow slice across the y direction that is centered upon the peak in $\rho(y)$ while excluding particles lying within a dis-
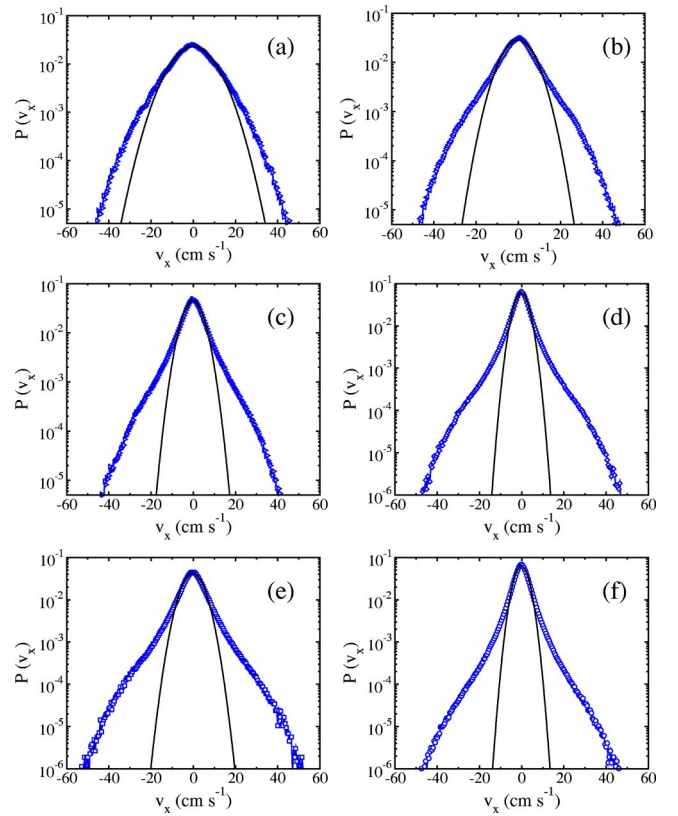
FIG. 11. (Color online) The velocity distribution functions $P(v_x)$ versus v_x on a log-linear scale. (a) $N_l=1$, $\beta=2.0$, (b) $N_l=2$, $\beta=2.0$, (c) $N_l=3$, $\beta=2.0$, (d) $N_l=4$, $\beta=2.0$, (e) $N_l=4$, $\beta=4.0$, (f) $N_l=5$, $\beta=4.0$. The solid curves are a least squares fit to a Gaussian form given by Eq. (17). Here the apparent deviations in the tails of the distribution functions are present.

tance of 3σ from the side walls. We utilize this ROI to ensure that large gradients in $\rho(y)$, and the clustering produced by the side walls, do not affect the measured VDFs. Each distribution correspond to $\sim 2\times 10^6$ unique velocities that are found within our ROI. The velocities of elastic particles follow a distribution given by the Maxwell-Boltzmann form

$$P(\mathbf{v})=(2\pi k_B T)^{-d/2}e^{-\mathbf{v}^2/2k_B T},\qquad(17)$$

where d is the dimensionality of the system and T is the temperature of the heat bath that the system is in contact with. Hence, if a system of particles is at equilibrium, its temperature determined by the width of the distribution of particle velocities. Equation (17) is fit to the data for the x-components of the velocities, and is shown on both linear and logarithmic scales (Figs. 10 and 11). We observe that the form given by Eq. (17) displays deviations both at low and high velocities. The distributions of velocities are normally displayed in a log-linear fashion to accentuate the tails of the VDF; however, this suppresses the deviations at low velocities. By plotting the distributions on a linear scale we display the more statistically significant deviations from Eq. (17).

In a recent experimental work [17], a two-dimensional collection of particles is driven into a steady state. Using
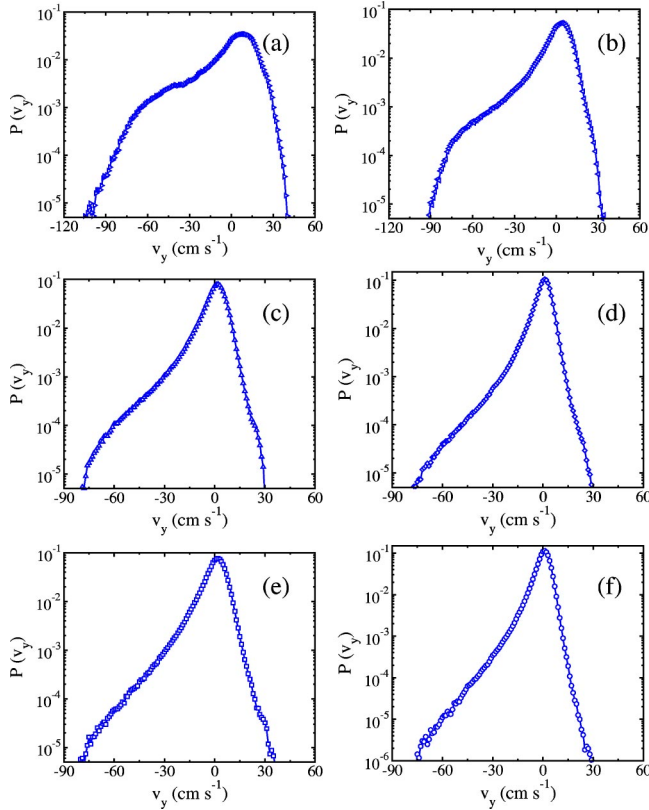
FIG. 12. (Color online) The velocity distribution functions $P(v_y)$ versus v_y on a log-linear scale. (a) $N_l=1$, $\beta=2.0$, (b) $N_l=2$, $\beta=2.0$, (c) $N_l=3$, $\beta=2.0$, (d) $N_l=4$, $\beta=2.0$, (e) $N_l=4$, $\beta=4.0$, (f) $N_l=5$, $\beta=4.0$. The large skewness in the distributions for the negative values of v_y is due primarily to the driving from the bottom wall. Particles that are moving in the $-y$ direction are leaving the moving wall.

analysis techniques that are similar to ours, the authors proposed a governing form for the VDF given by

$$R(\mathbf{v})=Ae^{-B|\mathbf{v}_x/T_x|^{-1.5}}, \qquad (18)$$

where A and B are constants and T_x is the x component of the granular temperature defined in Eq. (16). They claim to have seen a *universal* VDF which they parametrized by a single value, regardless of the system density or the value of the inelasticity of the particles. From our VDFs, whose corresponding densities range over an order of magnitude and where the average inelasticity varies by nearly a factor of two, we cannot find any single parameter fit that describes the overall form.

The VDFs for the y components, $P(\mathbf{v}_y)$ versus $\mathbf{v}_y$ for each $N_l\beta$ in our ROI are also measured [see Fig. 12(a–f)]. The VDFs are highly skewed by the asymmetry in the driving against the direction of gravity. To identify the effects that the asymmetry in $P(\mathbf{v}_y)$ has upon $P(\mathbf{v}_x)$, we have separated the $\mathbf{v}_x$ distributions by the sign of $\mathbf{v}_y$, i.e., $P(\mathbf{v}_x|+\mathbf{v}_y; -\mathbf{v}_y)$. We have found that the form for these conditional distributions are not affected by the sign of $\mathbf{v}_y$, however, we do note that their widths differ, with $\langle\mathbf{v}_x\rangle_{+\mathbf{v}_y}<\langle\mathbf{v}_x\rangle_{-\mathbf{v}_y}$.
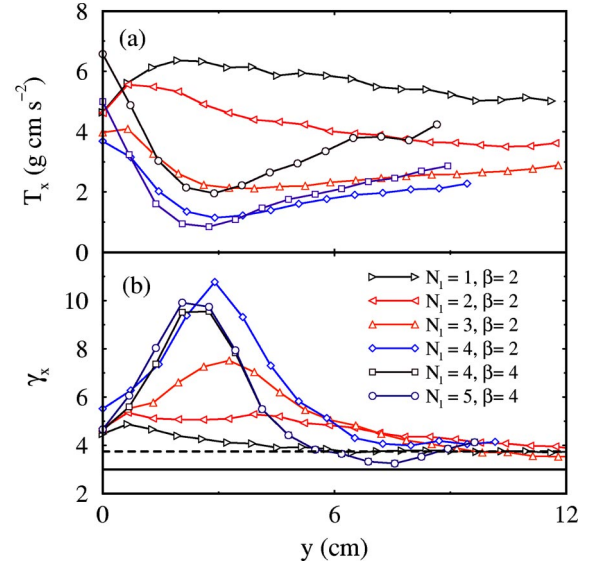

FIG. 13. (Color online) (a) The granular temperature $\frac{1}{2}m\langle\mathbf{v}_x^2\rangle$ as a function of distance from the driving wall for each $N_l\beta$. If the isothermal atmosphere condition was satisfied these would be constant values for all y above the peak in $\rho(y)$. For values of $N_l>2$ the temperatures follow a nonmonotonic form that has a distinct minimum. (b) The kurtosis γ_x measured from $P(\mathbf{v}_x)$ as a function of the distance from the driving. The values given by a Gaussian (solid line) and the form proposed in Eq. (18) (dashed) are only attained very far from the energy source.

We also measure the x component of the granular temperature T_x [see Eq. (16)], to probe the scaling behavior of the velocity distributions. Figure 13(a) shows the measured granular temperature as a function of distance from the driving wall. At low densities ($N_l\lesssim2$), $T_x(y)$ initially increases and then decays. In contrast, for ($N_l\gtrsim3$), $T_x(y)$ has a distinct minimum. We note that $T_x(y)$ never reaches a constant value and the minimum (maximum) does not correspond to the peak in $\rho(y)$.

To further show the nonuniversality of the VDFs, we plot the kurtosis as a function of distance from the driving wall. The kurtosis is obtained by the following:

$$\gamma=\frac{\langle v_x^4\rangle}{\langle v_x^2\rangle^2}. \qquad (19)$$

If the velocity distribution is a Gaussian then $\gamma=3$, shown by the solid line in Fig. 13(b), and if the distribution is given by Eq. (18) then $\gamma=3.576$. We find that the measured values for γ exceed the value for a Gaussian and also vary as a function of distance from the driving. This analysis is consistent with our previous results [21] and recent MD simulations of Brey and Ruiz-Montero [27] that closely mimic our experiment.

F. Equation of state

The equation of state for ideal gases relates the pressure to the temperature and the density,
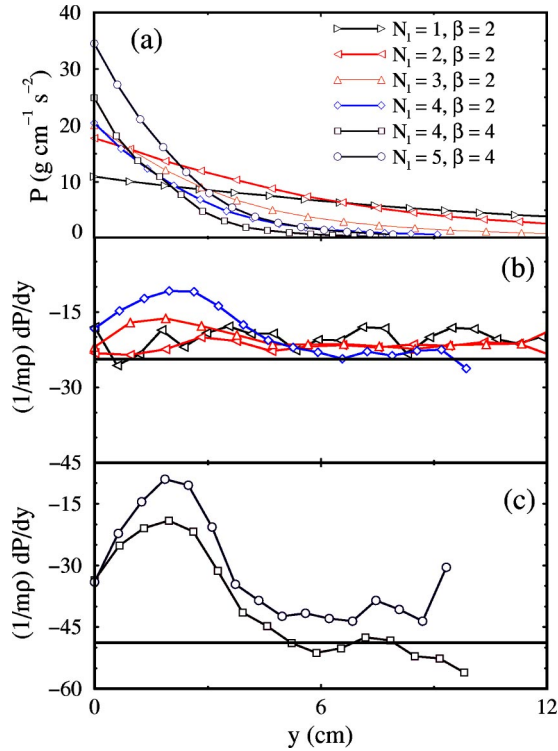
$$P=nk_BT, \qquad (20)$$

FIG. 14. (Color online) (a) The pressure $P(y) = \rho T$ as a function of y, the distance from the driving wall. (b) The ratio of the mass density to the granular pressure force $(1/m\rho)(dP/dy)$ as a function of distance from the driving wall. The solid line corresponds to g' for $\beta = 2°$. (c) The same as (b) for $\beta = 4°$. The obvious deviation for regions of high density show a breakdown of the simple treatment of the granular equation of state in regions of high density.

where n is the number density and k_B is Boltzmann's constant. If we assume that kinetic theory is valid for a granular gas, we can immediately relate the average squared speed, $\langle v^2 \rangle$ of the particles to the temperature,

$$m\langle v^2 \rangle = k_B T, \qquad (21)$$

for each degree of freedom. Figure 14(a) shows the pressure, $P = (nm/2)\langle v_y^2 \rangle$ as a function of distance from the driving wall. Due to the effects of gravity on the particles, the density should follow the well-known atmospheric law,

$$\rho(y) = \rho_0 e^{-mgy/T_y}, \qquad (22)$$

which assumes a constant temperature. We find that the temperature is not constant for any $N_l\beta$ [see Fig. 13]. This is also consistent with our observations of the density distributions in Sec. III A, where $\rho(y)$ deviates from the form of Eq. (22).

Momentum balance implies that the gradient of the pressure is related to n by the following equation:

$$\frac{dP}{dy} = -nmg, \qquad (23)$$

where m is the mass of a particle and g is the acceleration of gravity. Due to the nonvanishing gradient of temperature the general form of the pressure gradient must be taken into account

$$\frac{dP}{dy} = T_y \frac{dn}{dy} + n\frac{dT_y}{dy}. \qquad (24)$$

We find that Eq. (24) is indistinguishable from the numerical derivative of $d(nT_y)/dy$.

We have measured the pressure gradient acting on a particle held at a particular y by evaluating

$$-\left(\frac{T_y}{nm}\right)\frac{d(nT_y)}{dy} = g', \qquad (25)$$

where $g' = \frac{5}{7}g\sin(\beta)$. Figure 14(b) shows the left-hand side (lhs) of Eq. (25) for $\beta = 2$, and Fig. 14(c) for $\beta = 4$. The solid lines correspond to the values of g' with $\beta = 2,4$ found by utilizing Eq. (1) and the data in Fig. 2(b). We find that the measured values systematically overestimate the actual values for g' in the region where the density reaches it's maximum. Our interpretation assumes a dilute gas, therefore the deviations near the peak in $\rho(y)$ are not surprising.

To incorporate the effects due to increased density, we have obtained the pressure from the interpolated equation of state derived by Grossman, Zhou, and Ben-Naim [6],

$$P = nT_y \frac{n_c + n}{n_c - n}, \qquad (26)$$

where n_c is the close packing number density. Utilizing Eq. (26) to calculate the gradient of the pressure [Eq. (23)]. However, we find that the disagreement persists between the lhs of Eq. (25) and the measured value of g' near the peak in $\rho(y)$.

V. SUMMARY AND CONCLUSION

In this paper, we have presented a statistical analysis of an inelastic gas that is constrained to two dimensions. Utilizing high-speed digital image processing we perform long-time tracking over a broad range of densities. Not surprisingly, we observe that the statistical properties of inelastic gases deviate from expectations of the kinetic theory for smooth elastic particles. The most apparent discrepancies are found in the distribution of free paths and times and the distribution of particle velocities.

To characterize our system we measure the effective coefficient of restitution from the relative precollision and postcollision velocities of particles undergoing binary collisions. We find that the normal component of restitution and the energy inelasticity are not single-valued, but have a distribution of values even for the same impact parameters. The mean value of the normal components of restitution systematically decreases with the system density. We also find that the energy inelasticity can take on values greater than unity, demonstrating a transference of energy from the rotational to linear degrees of freedom. In a recent numerical work Barrat and Trizac have measured the projected one-dimensional co-

efficient of restitution Refs. [39,44] and the energy inelasticity. Their interpretation is that the coefficient of restitution and the energy restitution are random variables that characterize collisions, consistent with our findings.

The distribution of path lengths and free times are shown to have an overpopulation of the short distance and time bins. We have proposed an empirical form in Eqs. (7a) and (7b) which capture the overall behavior of the observed distributions of paths and times. By integrating these distribution functions, we are able to measure the mean free path and mean time. The average speed obtained from the speed distribution and from the mean free path and time are in close agreement. Inspired by these finding, Paolotti *et al.* [26] have reported similar results for the mean free time in a simulation that mimics our system.

Particle diffusion constants are measured from two independent long-time averaged correlation functions. The mean square displacement and the velocity autocorrelation function are calculated. By then performing least squares fitting and numerical integration to these quantities, respectively, the self diffusion over a broad range in density is calculated. We find that the diffusion constants are similar to that of a two-dimensional gas over this density regime. Therefore, long-time averaged correlation functions seem to accurately capture the diffusive properties of granular gases.

We find that the distribution of particle velocities perpendicular to the direction of driving does not have a universal form, but depends on both the density and the inelasticity. In addition, we find a distinct asymmetry in the VDFs parallel to the driving direction. We measure the granular temperature as a function of distance from the driving source and find nonmonotonic behavior. For low densities, the granular temperature has a distinct maximum and for high densities there exists a distinct minimum. The temperature inversion at higher densities has recently been described via granular hydrodynamics by Ramírez and Soto [45]. However, the crossover from $T(y)$ having a maximum (for low densities), to $T(y)$ with a minimum at high densities has not been discussed in any kinetic or hydrodynamic models.

By using kinetic theory and simple hydrodynamics we have tested the force balance between the gradient of the pressure exerted by a granular gas on a particle and the force due to gravity [Eq. (23)]. We find strong deviations in the regions of high density. A simple hydrodynamic form, that describes the behavior over all densities, is not yet available.

[1] H.M. Jaeger, S.R. Nagel, and R.P. Behringer, Rev. Mod. Phys. **68**, 1259 (1996).

[2] S. Chapman and T. Cowling, *The Mathematical Theory of Non-Uniform Gases* (Cambridge University Press, Cambridge, 1970).

[3] J.T. Jenkins and S.B. Savage, J. Fluid Mech. **130**, 187 (1983).

[4] P.K. Haff, J. Fluid Mech. **134**, 401 (1983).

[5] S. McNamara and W.R. Young, Phys. Fluids A **4**, 496 (1992).

[6] E.L. Grossman, T. Zhou, and E. Ben-Naim, Phys. Rev. E **55**, 4200 (1997).

[7] L.P. Kadanoff, Rev. Mod. Phys. **71**, 435 (1999).

[8] S. Warr, G.T.H. Jacques, and J.M. Huntley, Powder Technol. **81**, 41 (1994).

[9] A. Kudrolli, M. Wolpert, and J.P. Gollub, Phys. Rev. Lett. **78**, 1383 (1997).

[10] J.S. Olafsen and J.S. Urbach, Phys. Rev. Lett. **81**, 4369 (1998).

[11] T.P.C. van Noije and M.H. Ernst, Granular Matter **1**, 57 (1998).

[12] I. Goldhirsch, M.-L. Tan, and G. Zanetti, J. Sci. Comput. **8**, 1 (1993).

[13] A. Puglisi, V. Loreto, U.M.B. Marconi, A. Petri, and A. Vulpiani, Phys. Rev. Lett. **81**, 3848 (1998).

[14] S. Warr, J.M. Huntley, and G.T.H. Jacques, Phys. Rev. E **52**, 5583 (1995).

[15] S. Warr and J.M. Huntley, Phys. Rev. E **52**, 5596 (1995).

[16] R.D. Wildman, J.M. Huntly, and J.-P. Hansen, Phys. Rev. E **60**, 7066 (1999).

[17] F. Rouyer and N. Menon, Phys. Rev. Lett. **85**, 3676 (2000).

[18] J.S. Olafsen and J.S. Urbach, Phys. Rev. E **60**, R2468 (1999).

[19] W. Losert, D. Copper, J. Delour, A. Kudrolli, and J.P. Gollub, Chaos **9**, 682 (1999).

[20] A. Kudrolli and J. Henry, Phys. Rev. E **62**, R1489 (2000).

[21] D.L. Blair and A. Kudrolli, Phys. Rev. E **64**, 050301 (2001).

[22] T.P.C. van Noije, M.H. Ernst, E. Trizac, and I. Pagonabarraga, Phys. Rev. E **59**, 4326 (1999).

[23] S.J. Moon, M.D. Shattuck, and J.B. Swift, Phys. Rev. E **64**, 031303 (2001).

[24] I. Pagonabarraga, E. Trizac, T.P.C. van Noije, and M.H. Ernst, Phys. Rev. E **65**, 011303 (2002).

[25] J.S. van Zon and F.C. MacKintosh, e-print cond-mat/0205512.

[26] D. Paolotti, C. Cattuto, U.M.B. Marconi, and A. Puglisi, e-print cond-mat/0207601.

[27] J.Javier Brey and M.J. Ruiz-Montero, Phys. Rev. E **67**, 021307 (2003).

[28] A. Puglisi, V. Loreto, U.M.B. Marconi, and A. Vulpiani, Phys. Rev. E **59**, 5582 (1999).

[29] J.J. Brey, M.J. Ruiz-Montero, R. García-Rojo, and J.W. Dufty, Phys. Rev. E **60**, 7174 (1999).

[30] A. Baldassarri, U.M.B. Marconi, A. Puglisi, and A. Vulpiani, Phys. Rev. E **64**, 011301 (2001).

[31] W.A.M. Morgado and E.R. Mucciolo, Physica A (to be published), e-print cond-mat/0204084.

[32] A. Baldassarri, U.M.B. Marconi, A. Puglisi, and A. Vulpiani, Phys. Rev. E **64**, 011301 (2001).

[33] E. Livne, B. Meerson, and P.V. Sasorov, Phys. Rev. E **65**, 021302 (2002).

[34] E. Khain and B. Meerson, Phys. Rev. E **66**, 021306 (2002).

[35] M. Argentina, M.G. Clerc, and R. Soto, Phys. Rev. Lett. **89**, 044301 (2002).

[36] S. Luding, E. Clément, A. Blumen, J. Rajchenbach, and J. Duran, Phys. Rev. E **49**, 1634 (1994).

[37] S. McNamara and S. Luding, Phys. Rev. E **58**, 2247 (1998).

[38] L. Kondic, Phys. Rev. E **60**, 751 (1999).

[39] A. Barrat and E. Trizac, e-print cond-mat/0205546.

[40] C.E. Hecht, *Statistical Thermodynamics and Kinetic Theory* (Dover Publications, New York, 1998).

[41] M.P. Allen and D. Tildesley, *Computer Simulation of Liquids* (Oxford University Press, Oxford, 1996).

[42] B.J. Alder and T.E. Wainwright, Phys. Rev. Lett. **18**, 988 (1967).

[43] D. Henderson, Mol. Phys. **30**, 971 (1975).

[44] A. Barrat and E. Trizac, Phys. Rev. E **66**, 051303 (2002).

[45] R. Ramírez and R. Soto, e-print cond-mat/0210471.